POLITECNICO DI TORINO
Repository ISTITUZIONALE

Online Milliohm Variation Detector for Assessing Battery Internal Resistance

Original
Online Milliohm Variation Detector for Assessing Battery Internal Resistance / Maldonado, S., López, E., Ibarra, L., Galluzzi, R., Camacho, J., Ponso, A., Bonfitto, A.. - In: IEEE OPEN JOURNAL OF POWER ELECTRONICS. - ISSN 2644-1314. - ELETTRONICO. - 7:(2026), pp. 1256-1264. [10.1109/ojpel.2026.3682658]

Availability:
This version is available at: 11583/3009787 since: 2026-04-10T15:45:38Z

Publisher:
IEEE

Published
DOI:10.1109/ojpel.2026.3682658

Terms of use:

This article is made available under terms and conditions as specified in the corresponding bibliographic description in the repository

Publisher copyright

(Article begins on next page)

19 November 2026

IEEE Open Journal of
Power Electronics

Received 20 February 2026; accepted 7 April 2026. Date of publication 9 April 2026;
date of current version 22 April 2026. The review of this article was arranged by Associate Editor Marium Rasheed.

Digital Object Identifier 10.1109/OJPEL.2026.3682658

Online Milliohm Variation Detector for Assessing Battery Internal Resistance

SEBASTIAN MALDONADO [1] (Student Member, IEEE), EMILIO LÓPEZ [1], LUIS IBARRA [2] (Senior Member, IEEE), RENATO GALLUZZI [1] (Senior Member, IEEE), JESÚS CAMACHO [1] (Student Member, IEEE), ALBERTO PONSO [3], AND ANGELO BONFITTO [3]

[1]School of Engineering and Sciences, Tecnologico de Monterrey, Mexico City 14380, Mexico
[2]Institute of Advanced Materials for Sustainable Manufacturing, Tecnologico de Monterrey, Mexico City 14380, Mexico
[3]Department of Mechanical and Aerospace Engineering, Politecnico di Torino, 10129 Turin, Italy

CORRESPONDING AUTHOR: LUIS IBARRA (e-mail: ibarra.luis@tec.mx)

This work was supported in part by Tecnologico de Monterrey under Grant A00837152, in part by Research Stay program under Grant EI-AD25-042, Tecnologico de Monterrey, and in part by SECIHTI under Grant CVU:743126.

ABSTRACT This work introduces an online technique to detect variations at the milliohm-level of the equivalent internal resistance in a battery. This method is based on the voltage ripple generated by a DC-DC switching converter operating normally as its charger. It targets simple battery-associated hardware that measures only terminal voltage and output current, without additional excitation signals or specialized impedance instrumentation. An online dynamical model of the nominal converter–battery system replicates the baseline terminal voltage ripple generated under the same PWM input. The online-calculated covariance matrix for the measured and model-predicted ripple components is used to reveal variations in the internal resistance. Experimental validation, using a lead-acid battery together with a series-connected resistor network in the mΩ range to emulate an increase in internal resistance, showed smooth, monotonic dependencies between the proposed descriptors and resistance variations. This proof of concept suggests that converter-induced switching ripple could potentially support state-of-health estimation based on internal-resistance variations, using lightweight statistics compatible with typical charging hardware.

INDEX TERMS Battery state of health, lead-acid batteries, synchronous buck converters, switching ripple, embedded battery management, real-time estimation, equivalent-circuit modeling.

I. INTRODUCTION

State-of-health (SoH) monitoring governs safety, availability, and life-cycle economics in battery-powered systems, remaining a central objective and a parameter that must be estimated for battery management systems (BMSs) intended for practical deployment [1]. Battery aging, and therefore SoH degradation, commonly manifests itself as a decrease in total capacity along with an increase in equivalent internal resistance (EIR); this outcome reduces the available power and usable energy during operation [2]. In many applications, end-of-life (EoL) decisions depend on thresholds that rely on these parameters [3]. More precisely, a battery is considered to have reached EoL when its actual capacity has decreased by 20%—beyond which degradation increases exponentially [4]—or when its effective internal resistance has doubled its nominal value [5], [6].

Addressing the lack of online and in situ SoH diagnostics has technical and societal value. Timely, accurate SoH estimates enable adaptive charging, derating, and early fault detection, reducing overstress and extending battery life. At a higher level, reliable SoH indicators guide second-life decisions and safe transition of batteries to less demanding applications, where partially aged units can still be used without resorting to full laboratory characterization [7]. In the absence of practical online SoH diagnostics, operators often depend on coarse scheduling, conservative replacements, or slow capacity tests, which raise costs and can cause underutilization of remaining battery life.

The available SoH estimation methods are commonly grouped into direct measurement, model-based, data-driven, and hybrid categories [8]. Direct measurement techniques include Coulomb counting and Electro Impedance

© 2026 The Authors. This work is licensed under a Creative Commons Attribution-NonCommercial-NoDerivatives 4.0 License. For more information, see https://creativecommons.org/licenses/by-nc-nd/4.0/

Spectroscopy (EIS). The former measures the remaining battery capacity by integrating current during full discharge, but is impractical because it is time-consuming, the initial state is unknown, and the battery must be taken out of service. The EIS measures the internal impedance over a wide range of frequencies, effectively characterizing battery dynamics. However, it requires controlled excitation, long measurement times, and dedicated instruments, which interrupt normal battery operation. Consequently, direct measurement methods are not prevalent in SoH estimation proposals [9].

Electrochemical models use complex systems of partial differential equations to describe internal processes in detail and can accurately predict degradation from current and voltage profiles [10]. However, their complexity demands computational power incompatible with embedded platforms such as those used in Battery Management Systems (BMS). Therefore, electrochemical models must be simplified in practice, e.g., by approximating electrodes as single particles or using equivalent circuit models [11]. In their turn, data-driven SoH estimators have demonstrated high accuracy by deriving health indicators from measured trajectories [12]. Machine- and deep-learning methods can model complex relationships without prior knowledge, thereby avoiding errors from unmodeled effects. Nonetheless, they require extensive training datasets from lengthy and elaborate characterization tests, and discrepancies between laboratory and real-world conditions can reduce their accuracy.

Ideally, SoH estimation should run under practical field constraints, with limited sensing and during regular battery operation. While simplified EIS tests can be conducted in the 0.01–1,000 Hz band by injecting a disturbance into the DC-DC converter [13], a high performance digital signal processor is required to perform C-Morlet wavelet analysis. In contrast, artificial neural networks (ANNs) rely on simpler mathematical operations and can therefore be implemented on less powerful devices. In [14], real-time performance was achieved but required indirect time-dependent inputs, such as variations in state-of-charge (SoC) or available energy, so the method inherited the discussed drawbacks of direct measurement techniques. In its turn, in [15], specially designed excitation signals were necessary for battery characterization.

Building on the premise behind "internal resistance methods" for estimating SoH [16], this work introduces a battery analysis solution to estimate the EIR that can be easily integrated to the battery's charging hardware, therefore enabling real-time diagnostics through uninterrupted operation. This is achieved by using the converter-induced switching voltage ripple during the constant-current (CC) charging phase in a DC-DC converter. A dynamical model of the "healthy" combined converter-battery system is used to predict the switching voltage ripple under the same controlling PWM signal. By comparing the modeled and measured ripples, the method extracts covariance-based numerical descriptors that change as a function of the battery's EIR. These features provide an EIR-based indicator that can be evaluated online using only voltage measurements and limited computational effort. To demonstrate feasibility in a proof of concept manner, experimental validation was conducted on a lead-acid battery charged via a buck converter, where EIR increase is emulated through a series variable resistor.

The main contributions of this work are: (i) defining descriptors that relate switching-induced voltage ripple to EIR increase with a non-intrusive, real-time approach and (ii) proposing an embedded framework that couples a charger and real-time simulation with lightweight feature extraction to obtain SoH-relevant descriptors within microcontroller (MCU) constraints. While this work is centered in defining and validating a method to estimate EIR variations in a battery pack, it does not evaluate the relationship between EIR and SoH for a specific battery chemistry.

The remainder of this work is organized as follows. Section II describes the proposed solution, including the test bench, the buck-battery model and parameter identification, circuit design aspects, and the embedded estimator implementation. Section III reports the experimental results, Section IV addresses limitations and possible extensions, and Section V provides concluding remarks.

II. METHODOLOGY

In the proposed approach, a synchronous buck converter regulates a constant charging current to a lead-acid battery. At the battery terminals, the interaction between the converter dynamics and the battery impedance produces a voltage ripple at the switching frequency. At such a frequency—on the order of tens of kilohertz—the battery can be accurately modeled as an ohmic resistor in series with an open-circuit voltage source. Consequently, aging-induced variations in the EIR are expected to directly alter the ripple waveform. This effect is replicated by an external resistive network of a few milliohms. Although the anticipated variations are indeed minor, the primary objective of this study is to achieve informative and robust descriptors from these subtle differences.

The literature indicates that the EIR of a battery also depends on physical conditions such as internal temperature and SoC. Therefore, when using EIR as a proxy to estimate SoH, it is necessary to define reference values for temperature and SoC—or measure them—to prevent misinterpretations. As reported in [17], for a fixed temperature there is a low-variance region of EIR over a certain SoC interval, independent of the total charge processed during the battery's life—see Fig. 1. This pattern persists across battery temperatures, differing only by a resistance offset. To isolate the proposed tests from these effects, (i) the SoC was kept above 25% for all tests—assuming the resistance remains constant and does not vary with changes in SoC, see Fig. 1—and (ii) battery case and ambient temperatures were monitored with a Keysight U5855 A infrared thermal imager.

To turn the resistance-dependent ripple distortion into an indicator, an equivalent-circuit model of the buck-battery system is executed in real time. The model predicts the voltage ripple at the battery's terminals under the same PWM input. Rather than injecting additional perturbations, the estimator

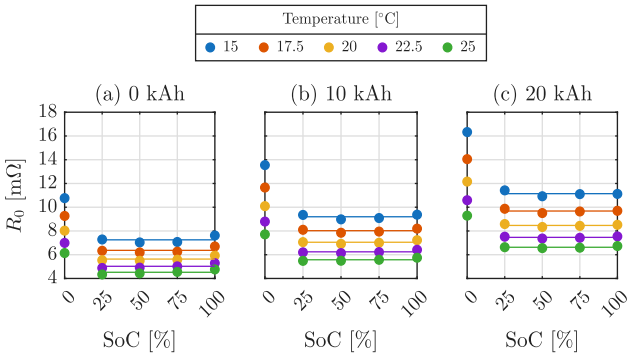


FIGURE 1. Battery internal resistance versus SoC for three moved-charge levels and five battery temperatures. Resistance at each SoC (dots) is compared with the average internal resistance over 25–100% SoC (solid line). Reproduced from Barcellona *et al.* [17].

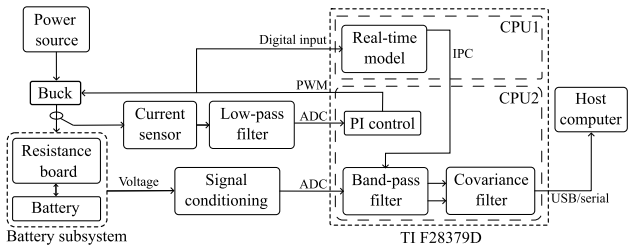


FIGURE 2. Block diagram of the proposed testbed.

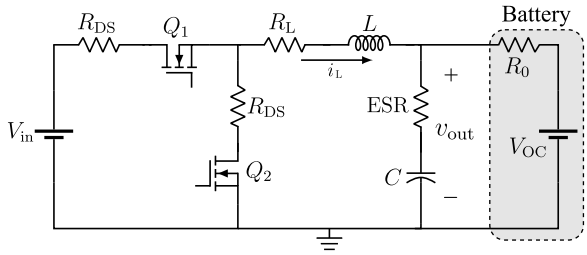


FIG. 3. Reference model of the buck converter with loss elements and a battery with internal resistance R_0 and open-circuit voltage V_{OC}.

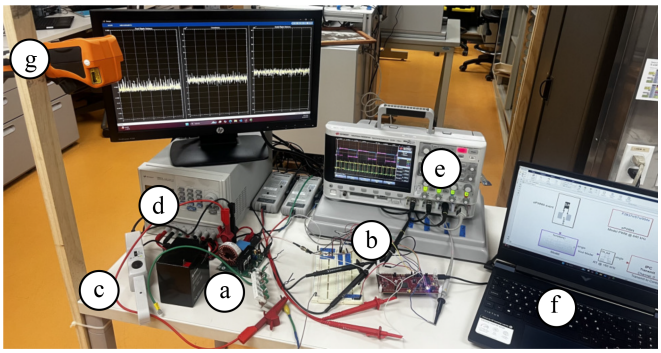


FIGURE 4. Experimental testbed comprising: ⓐ lead–acid battery, synchronous buck converter and resistors board; ⓑ acquisition and processing stage based on a MCU; ⓒ current sensor; ⓓ power supply; ⓔ oscilloscope; ⓕ host computer; ⓖ thermal camera.

compares the model-predicted and the measured output ripple that naturally takes place during the CC charging phase. These signals are expected to exhibit minor amplitude and phase shifts with varying EIR. In addition, the measured voltage is readily affected by noise, complicating the detection of genuine amplitude and phase differences. Consequently, measured and simulated voltage ripple signals are analyzed through their *online* covariance matrix, which directly yields filtered indicators of signal similarity. In addition, the covariance matrix fully defines the ellipse traced in a signal locus comparing the modeled ripple against the measured one, inherently including typical scalar indicators like variance and correlation, while also providing more interpretable—geometrical—descriptors. The covariance-based geometric representation yields major and minor semi-axis lengths and angle of rotation of an ellipse. These features change systematically with the EIR. The workflow is fully integrated and can operate on a low-cost dual-core MCU. One core runs the real-time dynamical model, while the other handles CC control and ripple acquisition. This second core also applies a moving covariance filter to the model and measurement ripple, producing geometric statistics for EIR estimation. The overall approach is depicted in the block diagram in Fig. 2.

A. TEST BENCH SETUP

Figure 3 shows the converter–battery circuit employed to derive the dynamic real-time model, incorporating non-ideal components that affect the voltage ripple waveform : inductor copper loss R_L, MOSFET on-resistance R_{DS} and capacitor equivalent series resistance ESR. The battery is modeled as an open-circuit voltage source, V_{OC}, in series with an ohmic internal resistance R_0. This first-order battery model is selected because of its simplicity and alignment with the estimation of the EIR . Moreover, it was observed to accurately reflect the high-frequency ripple behavior. In contrast, higher-order models that include polarization branches—charge-transfer and diffusion RC elements—mainly govern the mid to low frequency impedance and long-term voltage relaxation, with negligible contributions to the switching voltage ripple analyzed in this work [1], [18].

To corroborate this, the governing equations of first- and second-order models were implemented on different MCU cores, and their outputs were compared via separate digital-to-analog converters using an oscilloscope. Both models exhibited indistinguishable behavior, but the second order one took considerably longer execution time—530 ns against 165 ns, measured via GPIO toggling.

Experiments were conducted on the testbed shown in Fig. 4. A TI™ F28379D LaunchPad executed the real-time buck-battery model, the current control, and the data logging task. Current was measured with a Keysight 1146B 30-A clamp sensor (100 mV/A), followed by a passive RC low-pass filter, and digitized on a single-ended 12-bit analog-to-digital converter (ADC); acquisition of voltage ripple is later explained in Section II-C. A synchronous buck converter charged a 12-V,

TABLE 1. Characterization of Resistor Board Taps

Tap index	Mean [mΩ]	Std. dev. [μΩ]
1	9.766	113.24
2	14.786	74.87
3	19.040	23.815
4	22.495	71.436
5	27.911	93.604

4-Ah lead-acid battery at a rate of 200 mA. To this end, the converter was fed by a Keysight U8031 A power supply at 21 V.

An adjustable milliohm-range series resistor, implemented as a tap network on a custom board, was placed between the buck output and the battery to emulate series resistance variations, consistent with the nominal internal resistance of the battery of 35 mΩ. The use of this circuit facilitates an artificial increase of the EIR without having to age the tested battery pack. In the experiments, five distinct taps of this network were used, providing increments of about 5 mΩ. For each tap, the real resistance value was characterized by 1,000 samples using a Keithley DMM7510 digital multimeter with 100 nΩ resolution in the range of interest. The resulting mean and standard deviation of the resistance for each tap are shown in Table 1.

B. BUCK-BATTERY MODEL

A piecewise-linear model is adopted to explicitly represent the on/off states of the circuit, thus retaining the in-cycle ripple behavior [19]. Converter equations are obtained by applying Kirchhoff's laws to the ON/OFF states in Fig. 3.

Let T_s denote the switching period and D the duty cycle; they both define the binary PWM state

$$u(t) = \begin{cases} 1, & 0 < t < DT_s \\ 0, & DT_s \le t < T_s. \end{cases} \tag{1}$$

The differential equation governing the inductor current dynamics is given by

$$\frac{di_L}{dt} = \frac{V_{in}}{L}u(t) - \frac{R_{DS} + R_L + \frac{R_0\,\mathrm{ESR}}{R_0+\mathrm{ESR}}}{L} i_L(t) - \frac{R_0}{L(R_0+\mathrm{ESR})} v_C(t) - \frac{\mathrm{ESR}}{L(R_0+\mathrm{ESR})} V_{OC} \tag{2}$$

which reduces to the ON equation for $u = 1$ and to the OFF equation for $u = 0$. Similarly, the capacitor voltage dynamics are governed by

$$\frac{dv_C}{dt} = \frac{R_0}{C(R_0+\mathrm{ESR})} i_L(t) + \frac{1}{C(R_0+\mathrm{ESR})} v_C(t) + \frac{1}{C(R_0+\mathrm{ESR})} V_{OC} \tag{3}$$

and the terminal voltage across the battery follows directly:

$$v_{out}(t) = \frac{R_0\,\mathrm{ESR}}{R_0+\mathrm{ESR}} i_L(t) + \frac{R_0}{R_0+\mathrm{ESR}} v_C(t) + \frac{\mathrm{ESR}}{R_0+\mathrm{ESR}} V_{OC}. \tag{4}$$

TABLE 2. Identified Buck-Battery Model Parameters

Parameter	Symbol	Value
Inductance	L	439.68 μH
Capacitance	C	10.01 μF
Inductor series resistance	R_L	39.79 mΩ
MOSFET on-resistance	R_{DS}	357.56 mΩ
Capacitor equivalent series resistance	ESR	21.47 mΩ
Battery internal resistance	R_0	267.85 mΩ

The model parameters were identified with a two-stage genetic algorithm (GA) workflow. First, a GA was run to characterize the buck converter using a fixed resistive load and DC current steps—capturing steady state and transients—to fit $\{L, C, R_L, R_{DS}, \mathrm{ESR}\}$. Having these values fixed in the model, a GA was run to identify R_0 using the battery-CC model and voltage data from the charging operation. Note that R_0 accounts for the battery's nominal EIR—35 mΩ—as well as extra resistance from wiring and connectors. The resulting nominal values used in the embedded model are summarized in Table 2. The normalized root-mean-square error between the measured terminal-voltage (v_{meas}) and the model prediction (v_{mod}) was calculated over the identification windows to verify the validity of the fit:

$$\mathrm{NRMSE} = \sqrt{\frac{\sum_{k=1}^{N} (v_{meas}(k) - v_{mod}(k))^2}{\sum_{k=1}^{N} v_{meas}^2(k)}}. \tag{5}$$

Normalized errors of 0.579% for the buck-only identification and 0.091% for the battery-CC case were obtained.

For the on-chip execution, equations (2) and (3) were discretized through the forward Euler method using a fixed step h:

$$y(k+1) = y(k) + h\,f(k) \tag{6}$$

where $f(k)$ denotes the derivative of function y at step k, i.e., the right hand side of equations (2) and (3).

Applying (6) to (2) and (3), and letting $u(k) \in \{0, 1\}$ denote the PWM state at step k, the forward Euler updates are

$$i_L(k+1) = i_L(k) + h\left[\frac{V_{in}}{L}u(k) - \frac{R_{DS} + R_L + \frac{R_0\,\mathrm{ESR}}{R_0+\mathrm{ESR}}}{L} i_L(k) - \frac{R_0}{L(R_0+\mathrm{ESR})} v_C(k) - \frac{\mathrm{ESR}}{L(R_0+\mathrm{ESR})} V_{OC}\right] \tag{7}$$

$$v_C(k+1) = v_C(k) + h\left[\frac{R_0}{C(R_0+\mathrm{ESR})} i_L(k)\right.$$

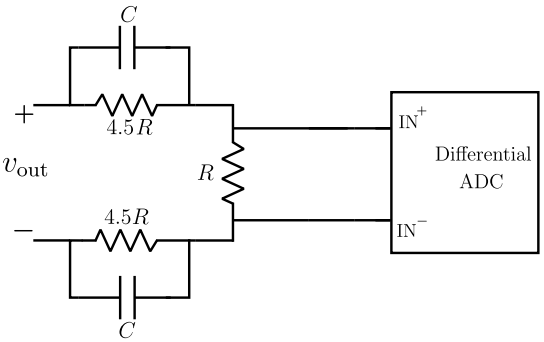


FIGURE 5. Frequency-dependent differential divider.

$$+\frac{1}{C(R_0+\mathrm{ESR})}v_C(k)\frac{1}{C(R_0+\mathrm{ESR})}V_{OC}\Bigg]. \tag{8}$$

C. CIRCUIT DESIGN CONSIDERATIONS

The battery terminal voltage was routed to the MCU via a frequency-dependent differential divider that attenuates the DC component while maintaining the switching ripple's amplitude—see Fig. 5. Two branches of $4.5R$ together with the center resistor R produce a DC gain $|H_{DC}| \approx R/(4.5R + R + 4.5R) = 1/10$, keeping V_{ADC} within a measurable range and improving the effective ripple definition in ADC counts. The capacitors shunt each arm to bypass the divider at the switching frequency f_s, $|Z_C| \ll 4.5R$, yielding an AC gain $|H_{AC}| \approx 1$. The differential connection improves robustness against common-mode disturbances and ground offsets.

This arrangement provides three simultaneous benefits: (i) it scales the DC component to fit the ADC input range, (ii) it preserves the high-frequency ripple used by the estimator, and (iii) it maintains isolation between the battery negative and the digital ground at the sensing point.

D. DEPLOYMENT AND REAL-TIME VALIDATION

Core 1 executed the real-time buck-battery model. The discrete-time realization of (7) and (8) was invoked by a timer-triggered interrupt at $f_{ISR} = 640$ kHz ($T_{ISR} = 1.56$ µs). A digital input, physically wired to the converter PWM signal, was sampled to obtain the switching state $u(t)$. GPIO toggling was used to verify real-time feasibility; the resulting pulse width was measured on an oscilloscope together with the PWM signal to capture the execution time and confirm that it remained within the switching period. The model's terminal-voltage output was computed in each interrupt, following (4), and sent via inter-processor communication to Core 2, down-sampled at a rate of 160 kHz. Core 2 implemented the CC control loop and voltage-ripple processing. The PWM module operated at $f_s = 20$ kHz and triggered the ADC start-of-conversion. At the end of conversion, the PI control was executed with the measured current, saturated to a duty cycle of 30–70%, and sent to the PWM module.

A second interrupt, triggered at 160 kHz, handled the voltage ripple acquisition and its comparison against the real-time model. The acquired values were fed through a digital bandpass filter with a 18–22 kHz band to preserve the switching ripple at f_s. To compute the online covariance matrix, Σ, the filtered pair, $X = \left[\check{v}_{meas}, \check{v}_{mod}\right]^\top$ was then processed by a moving covariance filter [20]:

$$\Sigma[n] = \Sigma[n-1] + \frac{1}{m}[(X[n] - \bar{X}[n])(X[n] - \bar{X}[n])^\top - (X[n-m] - \bar{X}[n-m])(X[n-m] - \bar{X}[n-m])^\top] \tag{9}$$

$$\bar{X}[n] = \bar{X}[n-1] + \frac{1}{m}[X[n] - X[n-m]] \tag{10}$$

where n is the discrete sample index and m denotes the length of the sliding window. The mean required in (9) is obtained using the standard *moving average* filter (MAF) (10). Observe that the general form of (9) matches that of (10); hence, its implementation can also rely on an MAF structure, with input $(X[n] - \bar{X}[n])(X[n] - \bar{X}[n])^\top$ [20]. In this context, the covariance is used as a measure of similarity; however, the MAF structure in (9)—a lowpass filter—also provides attenuation of high frequency components. For this study, $m = 24$ samples is the size of the moving window, corresponding to three periods of the switching ripple. Following the geometric-statistical formulation in [20], the covariance matrix, Σ, constructed from the predicted and measured samples is

$$\Sigma = \begin{bmatrix} \sigma(\alpha,\alpha) & \sigma(\alpha,\beta) \\ \sigma(\beta,\alpha) & \sigma(\beta,\beta) \end{bmatrix}, \qquad \sigma(\alpha,\beta) = \sigma(\beta,\alpha) \tag{11}$$

where terms α and β correspond to the model and measured ripple components, respectively. The major and minor axes of the ellipse arise from the eigenvalues of Σ:

$$\lambda_{\alpha,\beta} = \frac{1}{2}\left(\sigma(\alpha,\alpha) + \sigma(\beta,\beta) \pm \Gamma_1\right),$$
$$\Gamma_1 = \sqrt{\Gamma_2^2 + 4\left(\sigma(\alpha,\beta)\right)^2}, \quad \Gamma_2 = \sigma(\alpha,\alpha) - \sigma(\beta,\beta). \tag{12}$$

The associated eigenvectors determine the orientation of the ellipse:

$$V_{\alpha,\beta} = \left[\frac{\Gamma_2 \mp \Gamma_1}{2\sigma(\alpha,\beta)} \quad 1\right]^\top. \tag{13}$$

Therefore, the estimated semi-axes and rotation angle are computed as

$$\hat{a}_0 = \sqrt{2|\lambda_\alpha|}, \qquad \hat{b}_0 = \sqrt{2|\lambda_\beta|}, \qquad \hat{\rho}_0 = \angle V_\alpha \tag{14}$$

where $\hat{a}_0$ is the major axis, $\hat{b}_0$ is the minor axis and $\hat{\rho}_0$ denotes the orientation of the major axis with respect to the horizontal axis of the plane.

Briefly, these metrics encode the effect of the battery's internal resistance on the geometry of the v_{mod}-v_{meas} locus, and are used to extract a feature set sensitive to R_0 variations. In the current setup, the covariance matrix Σ is computed on

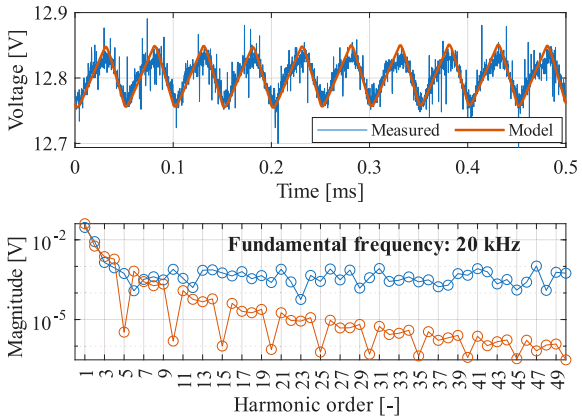


FIGURE 6. The upper panel shows the measured and model-predicted terminal-voltage ripple during constant-current charging. The lower panel shows the corresponding spectrum with the DC component removed. The model accurately captures the low-order harmonics. The additional high-frequency components in the measured signal arise from environmental noise, not filtered before entering the proposed system.

the MCU and transmitted via a serial interface to a host PC. Although Σ fully characterizes variations in R_0, the metrics in (14) are evaluated on the host for visualization.

E. TEST PROCEDURE

The charging procedure was performed 30 times for each EIR configuration, either with the buck converter connected directly to the battery terminals or via one tap of the external resistor board (see Table 1), resulting in 180 total tests. Note that the last tap of the resistor board corresponds to roughly twice the nominal internal resistance of the battery, representing a possible EoL condition according to literature [5]. After each iteration, the battery case and ambient temperatures were measured with the thermal camera to ensure all tests occurred under comparable thermal conditions. For each EIR setting, the host computer logged 600 consecutive outputs of the real-time covariance filter via a serial link. Each sample comprised the three components of Σ in (11): the measured ripple variance, the covariance between measured and model-predicted ripple, and the model-predicted ripple variance. The 600 samples per matrix element were averaged and used for subsequent analyses and reporting.

III. RESULTS

Figure 6 presents a sample time window of the measured voltage ripple alongside the modeled voltage ripple, as well as their spectral analyses. The modeled waveform is seen to track the measured voltage closely, primarily because it accurately represents the low-frequency components, while the higher-frequency portion appear to be dominated by noise. This shows that the identified model effectively reproduces the in-cycle behavior for subsequent statistical comparison. In contrast, Fig. 7 highlights the most informative descriptors as box plots against the added resistance. The first panel shows the variance of the measured ripple $\sigma(\beta, \beta)$, the second panel shows the covariance between measured and modeled

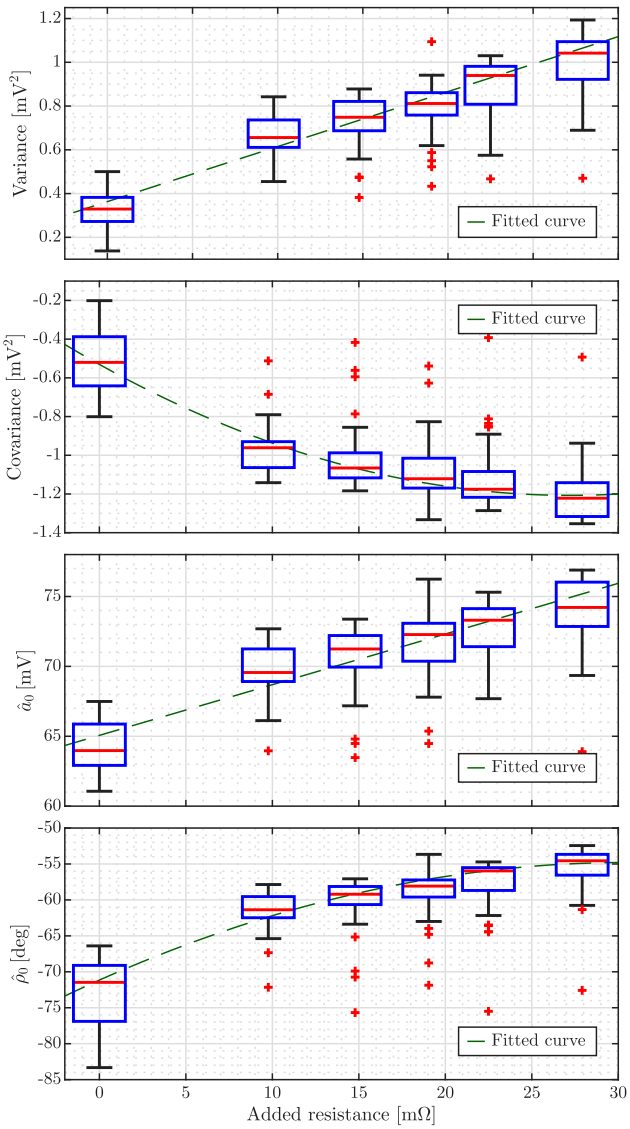


FIGURE 7. Boxplots of the measured ripple variance, the covariance between measured and modeled ripple, the major-axis length and the orientation angle of the fitted ellipse for each value of added series resistance. Dashed lines show least-squares fits to the feature medians.

ripple $\sigma(\alpha, \beta)$, the third panel shows the major-axis length of the fitted ellipse $\hat{a}_0$, and the fourth panel plots the orientation angle between the major axis and the measured-ripple axis $\hat{\rho}_0$. The variance of the modeled ripple and the minor-axis length $\hat{b}_0$ exhibited nearly constant, non-monotonic behavior across the tested range and is therefore omitted for clarity.

The whisker lengths and outliers show that the realizations are moderately dispersed. Nevertheless, the median of each feature changes systematically with increasing resistance. For the measured-ripple variance and major-axis length, the medians vary approximately linearly, so a first-degree polynomial was fitted to them. In contrast, both covariance and orientation angle exhibit slight curvature with increasing resistance, and their median trends are more accurately described by quadratic fits. The corresponding curves in Fig. 7

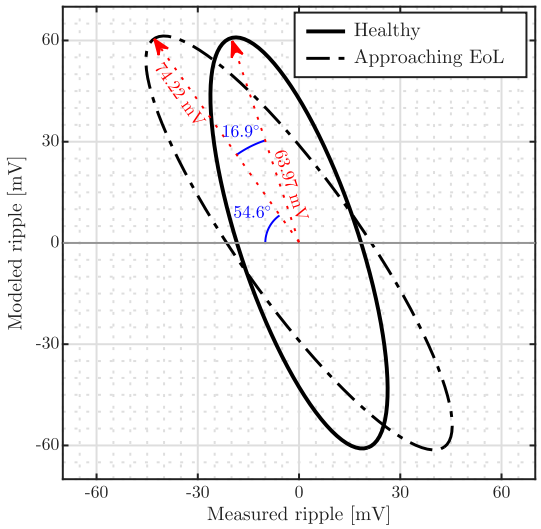


FIGURE 8. Ellipses reconstructed from the estimated parameters for the case without added resistance (healthy) and with 27.911 mΩ added series resistance (approaching EoL). Major axes' length and orientation are highlighted. Scales are equal to preserve the aspect ratio of the locus.

show that, despite sample-to-sample variability, the four selected descriptors yield smooth, monotonic relationships over the 0–30 mΩ range of added external resistance.

To better illustrate how increased resistance affects the ellipse representation, Fig. 8 shows ellipses reconstructed from the parameters in (14) for two characteristic cases: the healthy baseline with no added series resistance, and the condition with 27.911 mΩ added, deemed as a close-to-EoL condition for illustrative purposes. The axes correspond to the measured and modeled ripple components in millivolts. As expected from the trends in Fig. 7, the ellipse associated with the higher resistance exhibits a longer major axis (+10.25 mV or +16.02%) and a noticeable rotation (+16.9°), relative to the healthy case, reflecting an increase in ripple variance and the change in covariance as the EIR increases.

IV. DISCUSSION

The experimental results suggest that a converter-induced switching ripple can be interpreted as a signal that tracks changes in the EIR of the battery. As the milliohm-range series resistance increases, both the variance of the measured ripple and the major-axis length $\hat{a}_0$ of the fitted ellipse exhibit an approximate linear growth, while the covariance between the measured and modeled ripple becomes more negative as the resistance increases and the orientation angle $\hat{\rho}_0$ rotates in a consistent direction. Linear fits describe the behavior of the variance and $\hat{a}_0$ well, whereas quadratic fits capture the curvature observed in the covariance and $\hat{\rho}_0$. This suggests that simple low-order models are sufficient to map the proposed features to equivalent resistance.

The geometric view provided by the ellipse reconstruction in Fig. 8 helps interpret these trends. Both shapes give a clear visual separation between operating points whose EIR differs by approximately a factor of two, a level often associated with EoL in practice. From an implementation standpoint, results also show that the variance of the measured ripple alone already behaves as a strong scalar indicator: it is simple to compute, naturally monotonic with added resistance, and can serve as the primary feature for an embedded estimator, while additional descriptors such as $\hat{\rho}_0$ and the covariance can be incorporated to improve robustness or enable multi-feature calibration. Indeed, an exact phase-shift match between the two ripples at baseline is unnecessary, since the detected angle variation is always relative to the initial one.

Nonetheless, the study has limitations that frame how these findings should be interpreted. First, the rise in internal resistance was emulated using an external milliohm-range resistor board instead of by actually aging the battery. This approach isolates the effect of series resistance on the ripple geometry and makes the experiments repeatable in a controlled manner, but does not capture other degradation mechanisms which would potentially arise in naturally aged cells. Although this study primarily aimed to detect subtle ripple variations and to demonstrate diagnostic capability based on a charging-related feature—thus potentially enabling SoH estimation during normal operation—a natural next step is to test multiple batteries aged under well-controlled cycling and storage conditions. Experiments were also limited to a single lead-acid battery and to a single operating point. The degree to which the observed relationships generalize across different battery formats and chemistries remains an open question. This work only partly addresses this issue, building on previous studies that more broadly link EIR to SoH estimation in general. Exploring a broader design space would help determine whether the ripple-based indicators are portable, or application-specific calibration is required.

Overall, these results suggest that information already available in converter-driven dynamics can be reused for SoH estimation using lightweight statistics compatible with low-cost MCUs. Future work should validate these findings in naturally aged batteries, extend them to other operating conditions and chemistries, and convert the most robust descriptors into calibrated real-time SoH estimators for deployment in practical chargers and BMS hardware.

V. CONCLUSION

This work introduced the proof of concept of a ripple-based method for estimating the equivalent series resistance of the battery by comparing the predicted and measured terminal-voltage ripple of the model during constant-current charging with a synchronous buck converter. A real-time equivalent-circuit model, running alongside the CC controller on a low-cost MCU, enables extraction of statistical descriptors from converter-induced ripple, which experimentally tracked programmed variations in EIR emulated via an external milliohm-range board. The findings show that simple features derived from switching ripple during charging—particularly its variance, supported by interpretable elliptical descriptors such as the orientation angle—can underpin embedded SoH indicators without removing the battery from service, applying dedicated excitation, or using specialized instrumentation.

Future efforts will focus on validating this proof of concept with naturally aged batteries, extending it to a wider set of operating conditions and types of chemistry, and integrating calibrated resistance-to-SoH mappings into integrated charger and BMS implementations.

REFERENCES

[1] Y. Liu, L. Wang, D. Li, and K. Wang, "State-of-health estimation of lithium-ion batteries based on electrochemical impedance spectroscopy: A review," *Protection Control Modern Power Syst.*, vol. 8, no. 41, pp. 1–25, 2023.
[2] C. Huang and N. Li, "Fast health state estimation of lead–acid batteries based on multi-time constant current charging curve," *Electronics*, vol. 12, no. 21, 2023, Art. no. 4552.
[3] M. Mohsin, A. Picot, and P. Maussion, "A new lead-acid battery state-of-health evaluation method using electrochemical impedance spectroscopy for second life in rural electrification systems," *J. Energy Storage*, vol. 52, 2022, Art. no. 104647.
[4] A. Ponso, E. Cerva, N. Monticone, R. Sorace, A. Bonfitto, and A. Tonoli, "Efficiency and profitability of second life automotive batteries for renewable sources power plants," *J. Energy Storage*, vol. 145, 2026, Art. no. 119897.
[5] L. C. Casals, M. Rodríguez, C. Corchero, and R. E. Carrillo, "Evaluation of the end-of-life of electric vehicle batteries according to the state-of-health," *World Electric Veh. J.*, vol. 10, no. 4, 2019, Art. no. 63.
[6] D. Gong, Y. Gao, Y. Kou, and Y. Wang, "State of health estimation for lithium-ion battery based on energy features," *Energy*, vol. 257, Oct. 2022, Art. no. 124812.
[7] H. Velasco-Arellano, N. Castillo-Magallanes, N. Visairo-Cruz, C. A. Núñez-Gutiérrez, and I. Lázaro, "Parametric correlation analysis between equivalent electric circuit model and mechanistic model interpretation for battery internal aging," *World Electric Veh. J.*, vol. 15, no. 7, 2024, Art. no. 291.
[8] T. Wang, Z. Ma, S. Zou, Z. Chen, and P. Wang, "Lithium-ion battery state-of-health estimation: A self-supervised framework incorporating weak labels," *Appl. Energy*, vol. 355, Feb. 2024, Art. no. 122332.
[9] L. Chen et al., "State of health estimation of lithium-ion batteries based on equivalent circuit model and data-driven method," *J. Energy Storage*, vol. 73, Dec. 2023, Art. no. 109195.
[10] R. Xiong, L. Li, Z. Li, Q. Yu, and H. Mu, "An electrochemical model based degradation state identification method of lithium-ion battery for all-climate electric vehicles application," *Appl. Energy*, vol. 219, pp. 264–275, Jun. 2018.
[11] S. Hosseininasab, C. Lin, S. Pischinger, M. Stapelbroek, and G. Vagnoni, "State-of-health estimation of lithium-ion batteries for electrified vehicles using a reduced-order electrochemical model," *J. Energy Storage*, vol. 52, Aug. 2022, Art. no. 104684.
[12] Z. Wang, G. Feng, D. Zhen, F. Gu, and A. Ball, "A review on online state of charge and state of health estimation for lithium-ion batteries in electric vehicles," *Energy Rep.*, vol. 7, pp. 5141–5161, 2021.
[13] B. Liu, S. Qin, Z. Lyu, T. Wu, P. Huang, and Y. Pang, "On-line estimation for impedance of lithium-ion battery in DC-DC charger converter with step-response data and morlet wavelet," *Measurement*, vol. 257, Jan. 2026, Art. no. 118677.
[14] E. Ezemobi, A. Tonoli, and M. Silvagni, "Battery state of health estimation with improved generalization using parallel layer extreme learning machine," *Energies*, vol. 14, no. 8, Apr. 2021, Art. no. 2243.
[15] A. Ponso, A. Bonfitto, M. Silvagni, and S. Luciani, "Off-board testing device for battery diagnostics and market analysis for battery reuse," in *Proc. Vol. 1: 25th Int. Conf. Adv. Veh. Technol.*. Boston, Massachusetts, USA: American Society of Mechanical Engineers, Aug. 2023, Art. no. V001T01A009.
[16] S. G. Padder et al., "Data-driven approaches for estimation of ev battery soc and soh: A review," *IEEE Access*, vol. 13, pp. 35048–35067, 2025.
[17] S. Barcellona, S. Colnago, G. Dotelli, S. Latorrata, and L. Piegari, "Aging effect on the variation of li-ion battery resistance as function of temperature and state of charge," *J. Energy Storage*, vol. 50, 2022, Art. no. 104658.
[18] X. Tan et al., "Real-time state-of-health estimation of lithium-ion batteries based on the equivalent internal resistance," *IEEE Access*, vol. 8, pp. 56811–56822, 2020.
[19] J. Camacho, L. M. Ibarra, and P. Ponce, "Evaluating the influence of execution speed on real-time simulation accuracy: A buck converter case study," *IEEE Access*, vol. 13, pp. 15168–15177, 2025.
[20] L. Ibarra, "A fast convergence geometric–statistical approach for the estimation of three-phase electrical signal parameters," *IEEE Trans. Ind. Informat.*, vol. 21, no. 7, pp. 5536–5544, Jul. 2025.



SEBASTIN MALDONADO (Student Member, IEEE) currently working toward the B.Sc. degree in electronics engineering with Tecnológico de Monterrey, Mexico City Campus, Mexico. He has held internships in the telecommunications industry, focusing on mobile networks. His research interests include power electronics, power converters, real-time embedded systems, and control systems.



EMILIO LÓPEZ was born in Mexico City, Mexico, in 1993. He is currently working toward the B.S. degree in electronics engineering with Tecnológico de Monterrey, Mexico City Campus, Mexico. He was the part of professional internships in the hardware industry. He is currently an Embedded Systems Engineer. His research interests include power electronics, in particular, the use of DC-DC converters in real-time embedded systems.



LUIS IBARRA (Senior Member, IEEE) received the B.Eng. degree in mechatronics in 2011, and Ph.D. degree in intelligent control from Tecnologico de Monterrey, Mexico City, Mexico, in 2016. He is currently a Professor with the Institute of Advanced Materials for Sustainable Manufacturing, Tecnologico de Monterrey. He is a founding partner of a technology company. His research interests include power systems, automatic control, electric machinery, signal processing, and applied mathematics. Dr. Ibarra is a Member of the National Research Fellows System level 1 (SNII-1), SECIHTI, Mexico, and also a Member of the Mexican Academy of Sciences.



RENATO GALLUZZI (Senior Member, IEEE) received the M.Sc. and Ph.D. degrees in mechatronics from Politecnico di Torino, Turin, Italy, in 2010 and 2014, respectively. Since 2011, he has been an active collaborator with the Mechatronics Laboratoryt, Politecnico di Torino. He is currently a Research Professor with the School of Engineering and Sciences, Tecnologico de Monterrey, Monterrey, Mexico. His research interests include vibration control and damping systems, power actuators, electric machinery, and energy harvesting. Dr. Galluzzi is a Member of the National Research Fellows System level 1 (SNII-1), SECIHTI, Mexico.



JESÚS CAMACHO (Student Member, IEEE) received the B.Sc. degree in communications and electronics engineering from Instituto Politecnico Nacional ESIME Culhuacan, Mexico City, Mexico, in December 2015, and the M.Sc. degree in microelectronics engineering from SEPI-ESIME Culhuacan, Mexico City, in July 2018. He is currently working toward the Ph.D. degree with Tecnologico de Monterrey, Monterrey, Mexico From 2019 to 2022, he held a position in the telecommunications industry. His research interests include Power Electronics, Control Systems, System Dynamics, Real-Time Systems, and Simulation of Electric and Energy Systems.



ALBERTO PONSO received the B.Sc. and M.Sc. degrees in automotive engineering from Politecnico di Torino, Turin, Italy, in 2020 and 2022, respectively, where he has been currently working toward the Ph.D. degree in mechanical engineering, since 2022. His research interests include vehicle electrification, sustainable transportation, route planning of electric vehicles for grid integration and battery testing for state of health assessment and second-life addressing. He is working on these subjects in the Interdepartmental Center for Automotive Research and Sustainable Mobility (CARS) at Politecnico di Torino.



ANGELO BONFITTO received the Ph.D. degree in mechatronics from Politecnico di Torino, Turin, Italy, in 2010. He is currently an Associate Professor with the Department of Mechanical and Aerospace Engineering, Politecnico di Torino. He is Member of CARS@Polito, Interdepartmental Center for Automotive Research and Sustainable mobility. His research interests include mechatronic systems for automotive, modelling and control of hybrid and electric powertrains, technologies for assisted and autonomous driving, design and control of electromagnetic actuation for rotating machines.